Optica Applicata, Vol. XXV, No. 3, 1995

Moiré deflectometry as a method for measuring wave aberrations

M. ROTTENKOLBER*

ROTECH GmbH, Bergweg 47, 83123 Amerang, Germany.

Moiré deflectometry is a technique for measuring wave aberrations with high precision without using temporal coherent light. The sensitivity is adjustable and so it can close the gap between white light and interferometric methods. This is of major importance for measuring of optical surfaces like aspheric lenses. In moiré deflectometry usually two fringe patterns are generated, each providing a piece of information about the measured wavefront. The interpretation of these fringe patterns is more complex than in the case of ordinary interferograms. Therefore, in this paper, the properties of deflectograms, corresponding to various aberration types are analyzed numerically from computer generated deflectograms. Further, deflectograms of aberrations introduced by an aspherical surface are calculated. The ray matrix approach is proposed for calculation.

1. Introduction

Traditionally, the optical properties of lenses or optical surfaces are measured by interferometric methods. In interferometry, a wavefront with defined geometrical state is distorted by the object under investigation and then compared to a reference wave. The specimen may be a phase object (measured usually with a Mach–Zehnder interferometer), a lens, or a specular reflective surface (measured with a Twyman–Green interferometer). The main disadvantage of the interferometric method is that the sensitivity is not adjustable and it is in the range of wavelength of the light used. However, in many applications, *i.e.*, when measuring surfaces with strong asphericity, interferometry may be too sensitive and the fringe density is too high for further processing steps. The principle of two-wavelength interferometry may be used to avoid these disadvantages. Here, a synthetic wavelength is generated by a coherent source emitting two waves with different wavelength. However, this method is not frequently used since the requirements for stabilization of the light source are rather high [1].

Another possibility to overcome this problem is shearing interferometry. The light reflected from the surface is correlated with the light coming from the same surface but with a slight geometrical shift ("shearing"). The sensitivity is adjustable by the amount of shift. The carrier of the information is, like in interferometry, the phase of the optical

---

*M. Rottenkolber is a Ph.D. student at the Institute of Physics, Technical University of Wrocław, Poland, granted by TEMPUS PROGRAM.

wave. For this reason, the light used has to be temporally and spatially coherent. The principle of moiré deflectometry presented here (in literature well known as Talbot interferometry) is an incoherent analogy to shearing interferometry and is based on superposition of intensities.

The distored wavefront coming from the object causes deformation in the regular line structure of a grating. The shadow of this grating is compared to a reference grating. In this way, a moiré deflectogram is formed. As this method deals with the superposition of intensities there is no need for temporaly coherent light. Expensive light sources can be avoided and instead, cheap diode lasers with a high power output can be used. The sensitivity is adjustable and it is comparable to that of shearing interferometers.

2. Moiré deflectometry

2.1. Fundamentals

In deflectometry, a moiré effect is generated by a distored optical wavefront coming from the specular reflective object. The wavefront impinges on a pair of gratings that are placed at a certain distance from one another (Fig. 1).

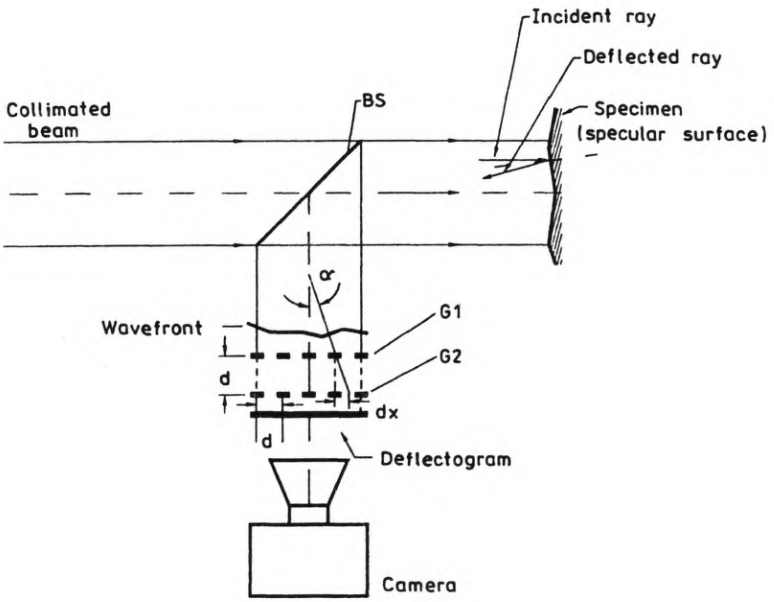

Fig. 1. Basic moiré deflectometer setup: a collimated beam illuminates the specular reflective surface. The light is reflected and directed on a pair of gratings G1 and G2. The resulting moiré pattern is observed directly behind grating G2 on a mat screen (deflectogram). The spacing of the two gratings is p, the distance between them is d. A light ray making an angle α with the optical axis produces a local displacement dx of the shadow of G1 on G2. The sensitivity in measuring of α is adjustable by varying the ratio p/d

The wavefront produces a distored shadow by passing through grating G1, which corresponds to the geometric properties of the initial wavefront. The shadow is compared to the second reference grating. The resulting superposition of intensities leads to a moiré pattern. This pattern is called moiré deflectogram [2]. Moiré deflectometry as a kind of grating shear interferometry has been well known for many years. It can be used for study of phase objects. It is realized by means of Talbot interferometers with a spatially coherent light source. Moiré methods in grating shearing interferometry are well documented in literature [3], [4].

The sensitivity is adjustable by varying the distance d between the gratings and the gratings pitch p. The local displacement δx of the shadow at G2, caused by a ray creating an angle α with the optical axis is given by $\delta x = \alpha d$. The accuracy in determination of the angle α depends on the distance d of the gratings and on the spatial frequency p^{-1} of the gratings. Assuming that the minimal detectable displacement is $dx = p$, one can find the minimum resolvable deflection angle $\alpha = p/d$.

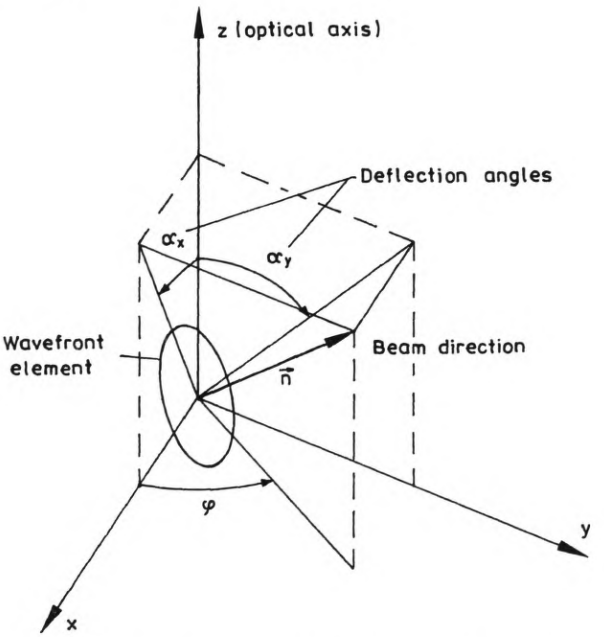

Fig. 2. Coordinate system used for calculation: the beam direction is given in spherical coordinates φ and α that can be expressed in terms of α_x and α_y. α_x lies in the xz-plane, α_y – in yz-plane. φ is used for rotation of the x'-plane around the z-axis to generate a 2D-surface, $\boldsymbol{n}$ – perpendicular to the wavefront element (see the text)

If Ronchi rulings are used and the two gratings are oriented parallel to each other, the resulting fringe pattern indicates contours of constant deflection angles, which are directly related to the partial derivatives of the impinging wavefront (*i.e.*, to the components of normals to the wavefront (Fig. 2)). The resolution of the deflection angles is limited by diffraction effects. Generally, the distance d between

the two gratings has to be chosen smaller than pa/λ. Only in this case do the lowest ($\pm$1st and zeroth) diffraction orders overlap and form a deflectogram (a is the aperture size).

When a pair of gratings with zero angle between the stripes is used, such a configuration is called an infinite fringe mode. In this case, a contour map of ray deflections with an increment p/d between adjacent fringes is observed in the moiré deflectogram.

2.2. Moiré effect for the infinite fringe mode

The information about the wavefront which enters grating G1 can be treated as a phase modulation at the location of G2 of the intensity transmission function T_1. This can be represented as the convolution of a locally displaced rect-function with a Dirac-comb

$$T_1(x,y) = \mathrm{rect}\left(\frac{2(x-\alpha(x,y)d)}{p}\right) * \sum_{n=-\infty}^{n=\infty} \delta(x-np). \tag{1}$$

This intensity distribution is superposed by multiplication with that of the reference grating G2

$$I(x,y) = \mathrm{rect}\left(\frac{2(x-\alpha(x,y)d)}{p}\right) * \sum_{n=-\infty}^{n=\infty} \delta(x-np)\left[\mathrm{rect}\left(\frac{2x}{p}\right) * \sum_{m=-\infty}^{m=\infty} \delta(x-mp)\right] \tag{2}$$

where the right-hand term in brackets denotes the intensity transmission function of the grating G2 that has not been distorted. Equation (2) serves as a basis for numerical calculations.

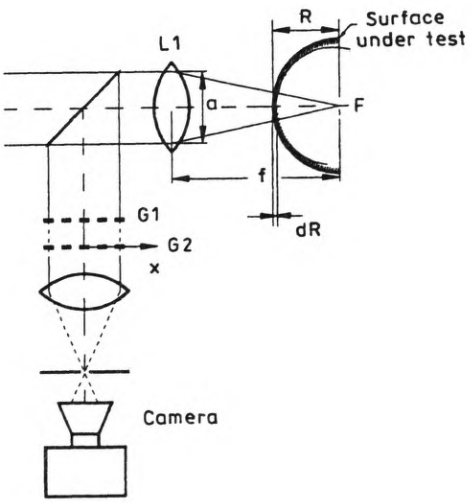

Fig. 3. Optical setup of moiré deflectometer for measuring curved surfaces

2.3. Measuring spherical surfaces

Figure 3 shows a possible setup for determination of the topography of a spherical or nearly spherical curved surface. An observation lens L1 is used to convert the spherically curved wavefront reflected from the investigated surface to a plane wave, which is then evaluated by a pair of gratings G1 and G2 [5]–[8]. If the centre of curvature S coincides with the focus F, no fringes will be visible in the deflectogram plane (in aberration free case). From the minimal resolvable angle (one fringe on the deflectogram) one can find a minimum difference dR in the radius R of the surface S: $dR \approx f^2 p/ad$.

3. First-order aberrations and their representation in the moiré deflectograms

Let us consider an arrangement shown in Figure 3 with a wavefront $W(x,y)$ targeting grating G1. In first order aberration theory, the wavefront distortion $W(x,y)$ can be expressed as [9]

$$W(x,y) = A(x^2+y^2)^2 + By(x^2+y^2) + C(x^2+3y^2) + D(x^2+y^2) + Ey + Fx \tag{3}$$

where A denotes the parameter for spherical aberration introduced by lens L1, B stands for coma, C – for astigmatism, D is the defocusing parameter, E and F are tilting parameters. The deflection angles α_x and α_y are given by the partial derivatives of W

$$\alpha_x = \frac{\partial W}{\partial x} = 4xA(x^2+y^2) + 2Bxy + 2Cx + 2Dx + \mathrm{F},$$
$$\alpha_y = \frac{\partial W}{\partial y} = 4yA(x^2+y^2) + 2B(x^2+3y^2) + 6Cy + 2Dy + E. \tag{4}$$

From Equation (4) we see that, except for the cases of pure coma and astigmatism, α_x and α_y are symmetrical, *i.e.*, the deflectograms are symmetrical, too.

Figure 4 shows the case of pure coma $A, C, D, E, F = 0, B = 1.0\ \mathrm{m}^{-2}$, calculated numerically from Eq. (2). Figure 4a is a 3-D plot of the wavefront $W(x,y)$. Figures 4b,c show the distribution of the deflection angles α_x and α_y. In Figure 4d and e, the calculated x- and y-deflectograms are displayed for the case of $p/d = 8 \times 10^{-5}$ and the aperture size 10 mm by 10 mm.

Figure 5 shows the deflectograms for pure spherical aberration ($A = 1600\ \mathrm{m}^{-3}$). For pure astigmatism or defocusing (parameters C, D) one can see from Eq. (4) that the deflectograms are in form of equally spaced lines, because of a linear dependence of the deflection angles on the x- or y-coordinate.

4. Wave aberrations introduced by an aspherical object

4.1. Ray matrix approach

We consider wave aberrations arising from an optical system shown in Figure 6. The observation lens L1 illuminates the specular reflective specimen. L1 is considered to

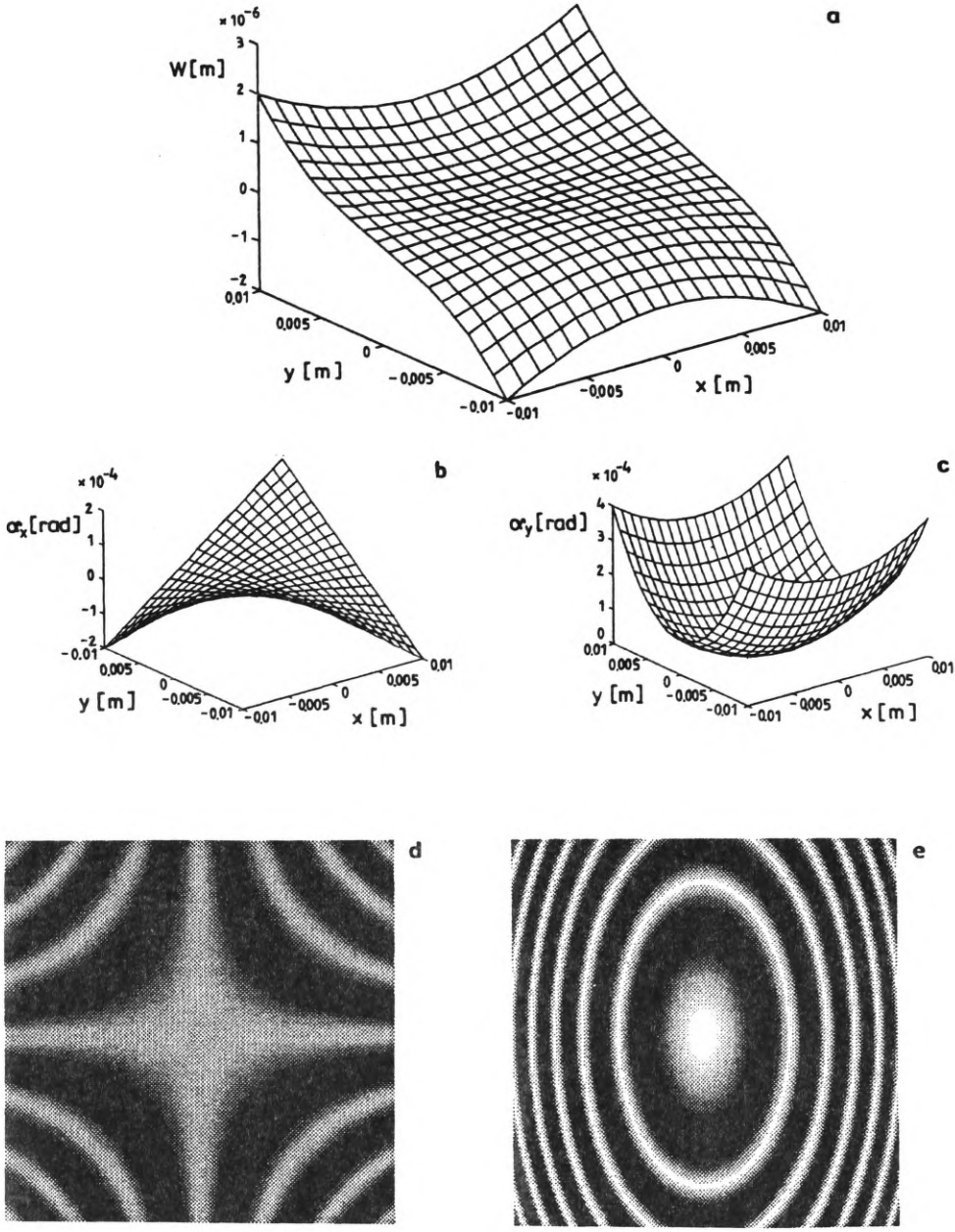

Fig. 4. Geometry of wavefront $W(x,y)$ for the case of pure coma, parameter $B = 1.0\ \mathrm{m}^{-2}$ (a). Distribution of deflection angle α_x (b). Distribution of deflection angle α_y (c). Computer generated x-deflectogram generated from Eq. (2), with pitch $p = 10$ μm, with distance between the gratings $d = 125$ mm (d). Computer generated y-deflectogram with the same parameters, in (d) and (e) the aperture size is 10 mm by 10 mm (e)

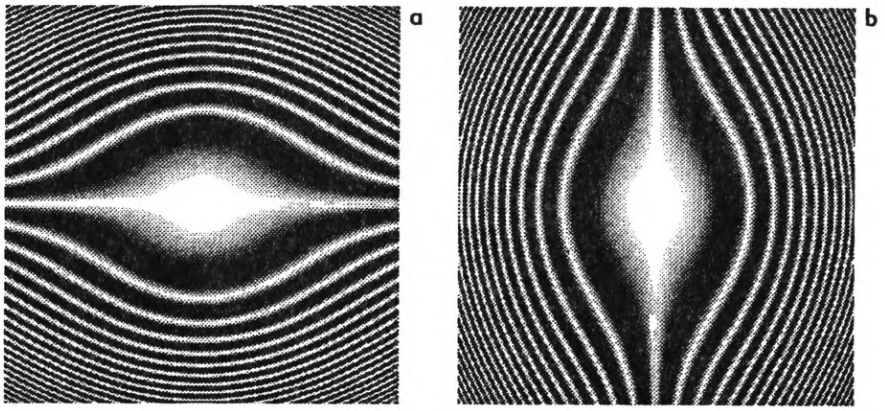

Fig. 5. Computer generated deflectogram for the case of pure spherical aberration, parameter $A = 1600$ m^{-3}. **a** – computer generated x-deflectogram generated from Eq. (2), pitch $p = 10$ μm, distance between the gratings $d = 125$ mm, **b** – computer generated y-deflectogram with the same parameters, the aperture size is 10 mm by 10 mm

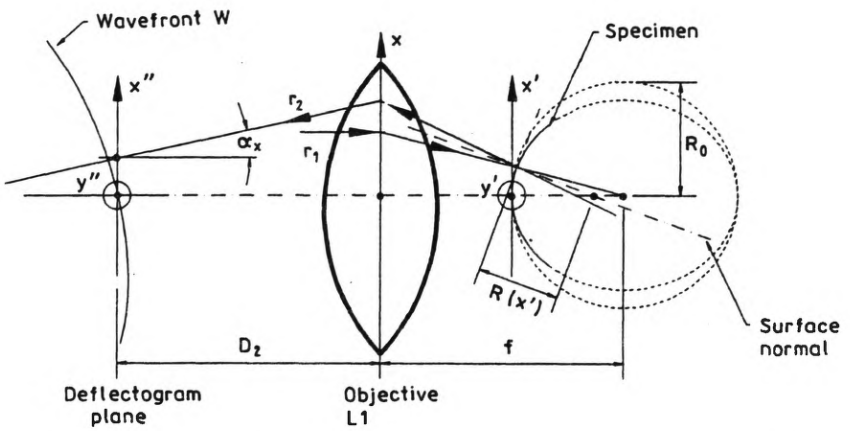

Fig. 6. Optical arrangement for calculating the relation between the radius of curvature and the corresponding deflection angle and location in the deflectogram plane. Coordinate systems: x-plane – principal plane of objective, x' – coordinate system for object, x'' – deflectogram plane. Parameters: r_1 – incident (collimated) ray vector, r_2 – resulting ray vector after double passing L1 and the object, α_x – deflection angle, R_0 – basic radius of curvature of the object on the optical axis, f – focal length of L1

be free from any optical errors. The light is reflected from the specimen and again passes L1. The wavefront $W(x,y)$ which is distorted by the object examined is evaluated by a pair of gratings and observed in the deflectogram plane x''. The specimen has nearly spherical surface and it has a local radius of curvature $R(x',y')$ and a basic radius of curvature R_0 on the optical axis. The centre of the circle with radius R_0 coincides with the focal point of L1.

We are interested in a relation between the geometry of the emerging wavefront $W(x,y)$ and the surface topography of the object examined. Deviations of an ideal plane wave can only arise if the surface geometry $R(x',y')$ of the specimen deviates

from an ideal spherical surface with the radius of curvature R_0. This relation will be calculated applying a ray matrix approach [10], *i.e.*, the relation between the variables x' and x'' (deflectogram plane) depending on $R(x',y')$ and, further, the dependence of the deflection angle α_x on the local radius of curvature $R(x',y')$ will be taken into consideration. We briefly illustrate the process for the one-dimensional case $(x,x',R(x'))$. In the paraxial approximation, the x and y coordinates can be treated independently.

In ray matrix approach, a ray is represented by a vector $r=(\alpha,x)$, where the first component α corresponds to the angle between ray and optical axis and the second component x represents the distance from the optical axis. Any changes introduced by an optical system (refraction, translation, reflection) result in a modified vector r_2, which can be calculated by multiplication with the system matrix S. The advantage of this approach is that more complicated optical systems can be treated in an easy way (a more general approach, which does not require paraxial approximation is shown in [11]).

In our case, the system matrix S is given by seven transmission stages: 1 — refraction of starting vector r_1 by lens L1 (L), 2 — translation x-plane $\rightarrow$ x'-plane ($T_{Hx'}$), 3 — refraction on specimen (M), 4 — reflection on specimen (R), 5 — translation x'-plane $\rightarrow$ x-plane ($T_{x'H}$), 6 — refraction by lens L1 (L), 7 — translation x-plane $\rightarrow$ x''-plane ($T_{Hx''}$):

$$S = T_{Hx''} L T_{x'H} R M T_{Hx'} L, \tag{5}$$

$$r_2 = S r_1 \tag{6}$$

where L is the ray matrix of the observation lens, $T_{x'H}$, $T_{Hx'}$ are the translation matrices from the principal plane HH' to the x'-plane and vice versa, $T_{Hx''}$ is the translation matrix from the principal plane HH' to the deflectogram plane, R stands for the reflection at the object. M is the matrix for the specimen and it can be represented by

$$M = \begin{bmatrix} 1 & \dfrac{2}{R(x')} \\ 0 & 1 \end{bmatrix}. \tag{7}$$

We examine only small deviations from an ideally spherical surface. For this reason, we can approximate $R(x')$ by

$$\frac{1}{R(x')} \approx \frac{1}{R_0} - \frac{\Delta R(x')}{R_0^2}. \tag{8}$$

Now, the matrix elements of the system matrix S can be calculated:

$$\begin{aligned} S_{11} &= 1 - 2\Delta R\left(\frac{1}{R_0} - \frac{1}{f}\right), \\ S_{12} &= -\frac{2\Delta R}{f^2}, \\ S_{21} &= D_2 S_{11} + \frac{2f^2}{R_0} - 2f - 2\Delta R\left(1 - \frac{f}{R_0}\right)^2, \end{aligned} \tag{9}$$

$$S_{22} = D_2 S_{12} + 1 - 2\Delta R\left(\frac{1}{R_0} - \frac{1}{f}\right), \tag{9}$$

R_0 is the basic radius of curvature of the specimen on the optical axis, D_2 is the distance between the deflectogram plane and the principal plane of objective L1, f is the focal length of the objective.

The deflection angle α_x between optical axis and the resulting ray vector r_2 can be derived from Eq. (9) and given by

$$\alpha_x = S_{12} x = -\frac{2\Delta R(x')}{f R_0} x'. \tag{10}$$

The relation between x'' and x' is described by the following formula:

$$x'' = S_{22} \frac{f}{R_0} x'. \tag{11}$$

From Equations (10) and (11) we are able to map the change in radius of curvature onto the deflection angle and the location in the deflectogram plane. This solution can be expanded to the general 2-D case, if the x-, x'- and x''-axes are rotated around the z-axis by an angle φ (Fig. 2).

4.2. Specimen with the 2nd order elliptical surface

Now, as an example the influence of a 2nd order elliptical surface on the properties of the x and y-deflectograms is discussed. As shown in Eqs. (9)–(11), the knowledge about the difference in radius of curvature ΔR for determining the deflection angles is required. When we restrict our considerations to 2nd order elliptical surfaces, R_2 and ΔR for the $x'z$-plane will be given as:

$$R_2(\vartheta, \varphi) = R_2 \sqrt{\cos^2 \vartheta + \frac{R_1^2(\varphi)}{R_2^2} \sin^2 \vartheta},$$

$$\Delta R(\vartheta, \varphi) = R_0 - R_2(\vartheta, \varphi) \tag{12}$$

with $\vartheta \approx -\frac{x'}{R_0}$. From Eq. (12) and radius function $R_1(\varphi)$ which describes the rotation around the z-axis, we can construct any ellipsoid with the three main axes $R_1(\varphi = 0)$ (radius in direction of the x'-axis), $R_1(\varphi = \pi/2)$ (radius in direction of the y'-axis) and $R_2(\varphi = 0, \vartheta = \pi)$ (radius on the z-axis). For the simulations shown below, $R_1(\varphi)$ was chosen to be in the following form:

$$R_1(\varphi) = \sqrt{r_1^2 \cos^2(\varphi + \varepsilon) + r_2^2 \sin^2(\varphi + \varepsilon)}. \tag{13}$$

In order to gain more knowledge concerning the interpretation of deflectograms, the transmission of basic aberration types into the deflectograms was studied by numerical generation of deflectograms. Depending on the type of aberration one gets different forms of symmetry in the single deflectogram and in both the x- and y-deflectograms. Table summarizes the parameter values for simulations 1–4.

Overview of the parameters used in the simulations

Sim.	$R_1(\vartheta)$, rotation around z-axis	$R_2(\vartheta)$, function in x'z-plane	R_0, basic radius	p/d
1	Eq. (13), $r_1 = 7.98$ mm, $r_2 = 7.86$ mm $\varepsilon = 0$ (see Fig. 8)	Eq. (12), $R_2 = 7.86$ mm	$R_0 = 7.86$ mm	$2 \cdot 10^{-5}$
2	Eq. (13), $r_1 = 7.98$ mm, $r_2 = 7.86$ mm $\varepsilon = \pi/4$ (see Fig. 8)	Eq. (12), $R_2 = 7.86$ mm	$R_0 = 7.86$ mm	$2 \cdot 10^{-5}$
3	$R_1 = \text{const} = 7.98$ mm, $\varepsilon = 0$	Eq. (12), $R_2 = 7.86$ mm	$R_0 = 7.86$ mm	$2 \cdot 10^{-5}$
4	$R_1 = \text{const} = 7.80$ mm, $\varepsilon = 0$	Eq. (12), $R_2 = 7.87$ mm	$R_0 = 7.86$ mm	$2 \cdot 10^{-4}$

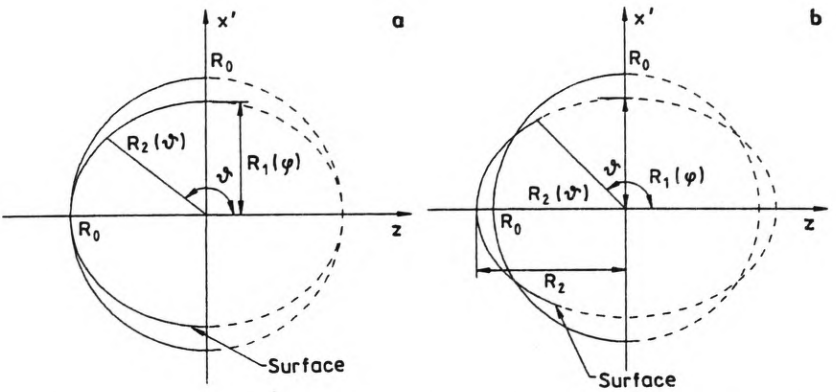

Fig. 7. Model for simulations 1–3, the specimen has a radius of curvature R_0 on the optical axis z (second main axis of the ellipse), the origin of the coordinate system coincides with the focal point of the observation lesn L1, the first main axis of the ellipse is given by $R_1(\varphi)$, which is variable when rotating around the z-axis (for the function $R_1(\varphi)$, see the text). The rotated surface forms an ellipsoid (a). Model for simulation 4, the second main axis has a length R_2 and differs from R_0 (b)

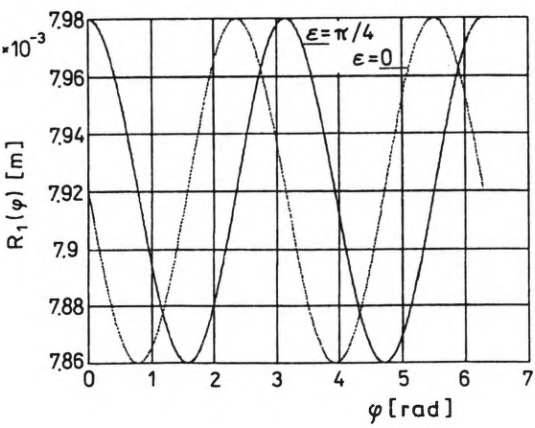

Fig. 8. Radius function $R_1(\varphi)$ for simulations 1 and 2, the solid function produces a surface with 90°-astigmatism ($\varepsilon = 0$), the dotted curve is used for producing a 45°-astigmatism ($\varepsilon = \pi/4$)

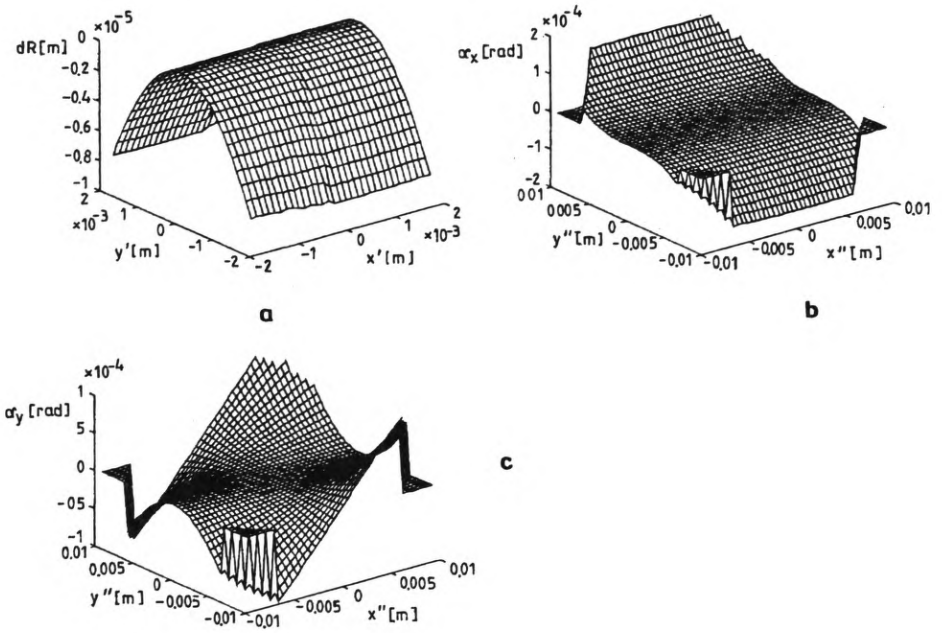

Fig. 9. Difference in radius of curvature ΔR for simulation 1 (a). 3D-plot of x-deflection angle α_x as calculated from Eqs. (10) and (11) (b). 3D-plot of y-deflection angle α_y (c)

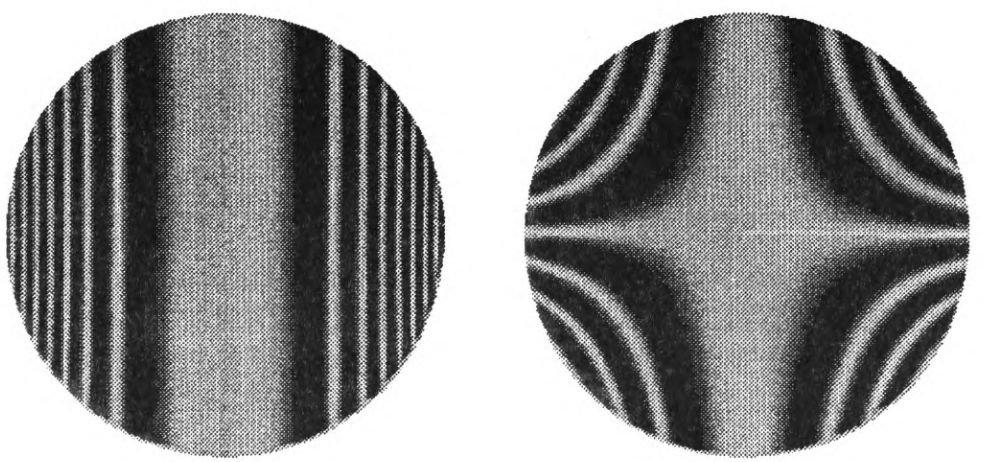

Fig. 10. x- and y-deflectograms for simulation 1 — the specimen is aspherical ("deformed" ellipsoid), the rotation function $R_1(\varphi)$ is given by: $R_1(\varphi) = \sqrt{r_1^2\cos^2\varphi + r_2^2\sin^2\varphi}$, with $r_1 = 7.98$ mm, $r_2 = 7.86$ mm, the aperture diameter is 30 mm, the ratio $p/d = 2{\cdot}10^{-5}$, $R_2 = R_0 = 7.86$ mm

The models for the generation of the surface are illustrated in Figures 7a and b. The surface has a radius of curvature R_0 on the optical axis z (second main axis of the ellipse), the origin of the coordinate system coincides with the focal point of the observation lens L1, the first main axis of the ellipse is given by $R_1(\varphi)$, which is

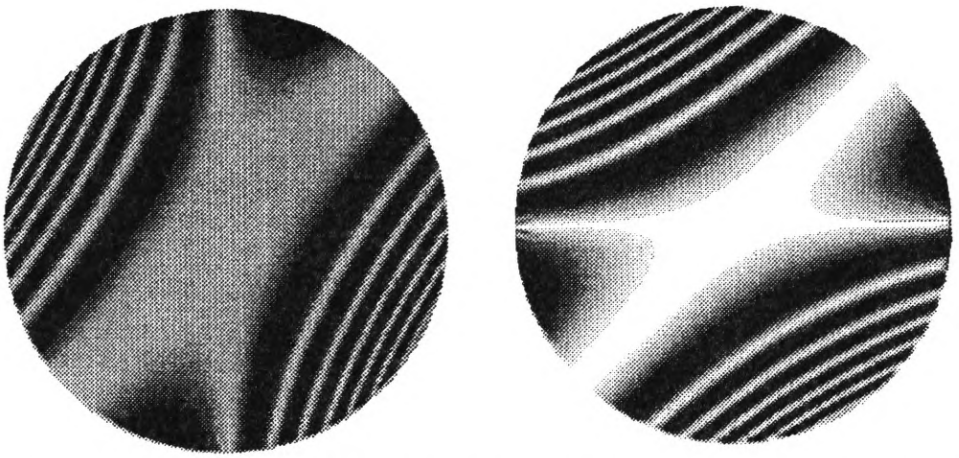

Fig. 11. x- and y-deflectograms for simulation 2, the specimen is aspherical in φ ("deformed" ellipsoid), the rotation function $R_1(\varphi)$ is given by: $R_1(\varphi) = \sqrt{r_1^2\cos^2(\varphi+\pi/4)+r_2^2\sin^2(\varphi+\pi/4)}$, with $r_1 = 7.98$ mm, $r_2 = 7.86$ mm, the aperture diameter is 30 mm, $p/d = 2{\cdot}10^{-5}$, $R_2 = R_0 = 7.86$ mm

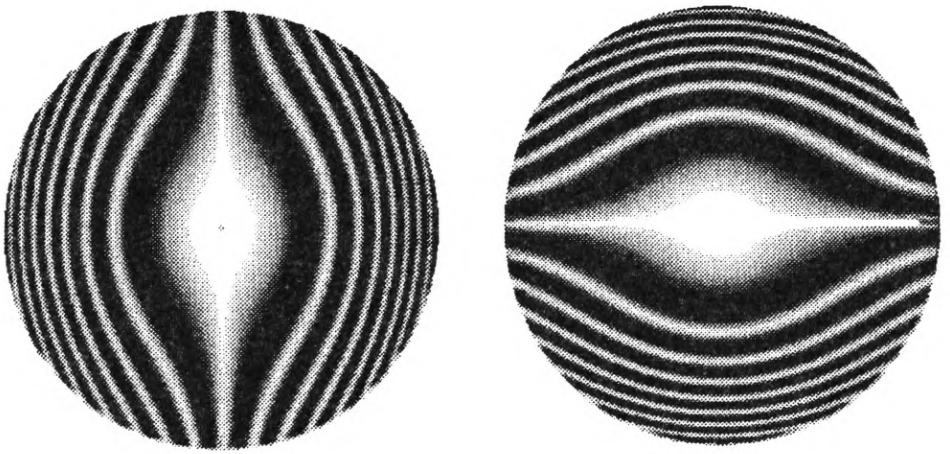

Fig. 12. x- and y-deflectograms for simulation 3, the specimen is aspherical in φ (symmetrical ellipsoid), the rotation function $R_1(\varphi)$ is given by: $R_1(\varphi) = \text{const} = 7.98$ mm, the aperture diameter is 30 mm, $p/d = 2{\cdot}10^{-5}$, $R_2 = R_0 = 7.86$ mm

variable when rotating around the z-axis. Figure 7b shows the model for simulation 4, the second main axis has a length R_2 and differs from R_0.

The function R_1 for simulations 1 and 2 is plotted in Fig. 8. The solid function produces a surface with 90°-astigmatism, the dotted curve is used for producing a 45°-astigmatism.

Figure 9a shows the difference in radius of curvature ΔR for simulation 1 (90°-astigmatism). In Figure 9b, the 3D-plot of x-deflection angle α_x calculated from Eqs. (10) and (11) is demonstrated. The 3D-plot of y-deflection angle α_y is drawn in Fig. 9c.

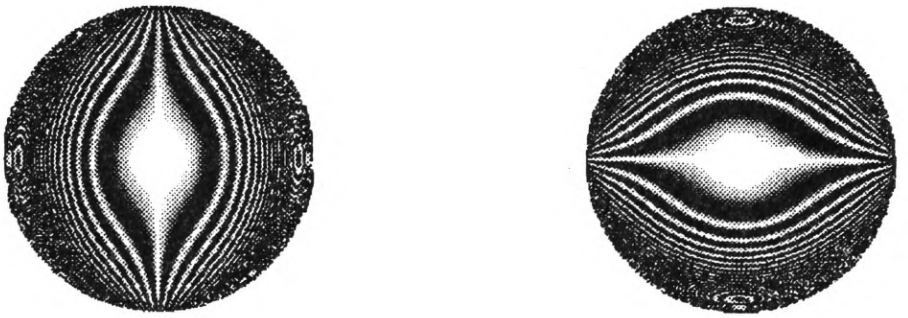

Fig. 13. x and y-deflectograms for simulation 4. The specimen is aspherical (symmetrical ellipsoid), the rotation function $R_1(\varphi)$ is given by: $R_1(\varphi) = \text{const} = 7.80$ mm, the aperture diameter is 30 mm, $p/d = 2{\cdot}10^{-4}$, $R_2 = 7.87$ mm, $R_0 = 7.86$ mm. The deflectograms appear smaller because of different radius of curvature on the optical axis (Fig. 7b). The low density fringe spacing in the outer region (horizontal in the x-deflectogram) indicates locations where the ellipsoid intersects the sphere with radius R_0

In Figure 10, we see x-and y-deflectograms for simulation 1 (90° astigmatism). The specimen is aspherical ("deformed" ellipsoid). The rotation function $R_1(\varphi)$ is given by $R_1(\varphi) = \sqrt{r_1^2\cos^2\varphi + r_2^2\sin^2\varphi}$, with $r_1 = 7.98$ mm, $r_2 = 7.86$ mm, the aperture diameter is 30 mm, the ratio $p/d = 2\times10^{-5}$, $R_2 = R_0 = 7.86$ mm. Both deflectograms show symmetry but there is no symmetry between them.

Figure 11 presents the x- and y-deflectograms for simulation 2 (45° astigmatism). The object is aspherical, the rotation function $R_1(\varphi)$ is given by: $R_1(\varphi) = \sqrt{r_1^2\cos^2(\varphi+\pi/4) + r_2^2\sin^2(\varphi+\pi/4)}$, with $r_1 = 7.98$ mm, $r_2 = 7.86$ mm, the aperture diameter is 30 mm, $p/d = 2\times10^{-5}$, $R_2 = R_0 = 7.86$ mm.

Figure 12 demonstrates as an example a symmetrical ellipsoid (simulation 3), the specimen is aspherical, the rotation function $R_1(\varphi)$ is given by: $R_1(\varphi) = \text{const} = 7.98$ mm, the aperture diameter is 30 mm, $p/d = 2\times10^{-5}$, $R_2 = R_0 = 7.86$ mm.

In Figure 13, the result for a distorted symmetrical ellipsoid is illustrated. The object is aspherical (symmetrical ellipsoid), the rotation function $R_1(\varphi)$ is given by $R_1(\varphi) = \text{const} = 7.80$ mm, $R_2 = 7.87$ mm, the aperture diameter is 30 mm, $p/d = 2\times10^{-4}$, $R_0 = 7.86$ mm. The deflectograms appear smaller because of different radius of curvature on the optical axis. The low density fringe spacing in the outer regions (horizontal in the x-deflectogram) indicates the locations where the ellipsoid intersects the sphere with radius R_0 (Fig. 7b).

5. Conclusions

In this paper, the principle of moiré deflectometry for measurement of wavefront aberrations is briefly discussed. When measuring aspherical optical surfaces, for example, contact lenses or the human cornea, it is necessary to find a relation beetwen the local radius of curvature and the deflection angles, respectively, as well as to find a relation between the degree of distortion of the wavefront depending on

the properties of the object under study. A ray matrix approach was applied to solve this problem. The computer generated moiré deflectograms for different types of aberrations can serve as a basis for further examinations of real optical surfaces. The results presented here can be useful for the evaluation of deflectograms obtained experimentally.

Acknowledgements – The author would like to thank Dr hab. H. Podbielska, Technical University of Wrocław, Poland, for constant encouragement and many helpful discussions during preparation of this paper.

References

[1] GERSTNER K., TSCHUDI T., Opt. Eng. **33** (1994), 2692.
[2] KAFRI O., *The Physics of Moirė Metrology*, Wiley, New York 1990.
[3] PATORSKI K., *The self-imaging phenomena and its applications*, [In] *Progress in Optics*, Vol. 27, [Ed.] E. Wolf, North-Holland, Amsterdam 1989, pp. 3–108.
[4] PATORSKI K., *Handbook of the Moirė Fringe Technique*, Elsevier Sci. Publ., Amsterdam 1993.
[5] KAFRI O., GLATT I., Appl. Opt. **27** (1988), 351.
[6] KAFRI O., LIVNAT A., Appl. Opt. **20** (1981), 3098.
[7] GLATT I., KAFRI O., Appl. Opt. **26** (1987), 2507.
[8] KEREN E., KRESKE K., KAFRI O., Appl. Opt. **27** (1988), 1383.
[9] BORN M., WOLF E., *Principles of Optics*, Pergamon Press, Oxford 1970.
[10] KLEIN M. V., FURTAK T. E., *Optik*, Springer-Verlag, Berlin 1988.
[11] ROTTENKOLBER M., PODBIELSKA H., Proc. SPIE **2390** (1995), 142.

Received May 12, 1995
in revised form June 21, 1995